The type III effector EspF coordinates membrane trafficking by the spatiotemporal activation of two eukaryotic signaling pathways

Neal M. Alto,[1] Andrew W. Weflen,[3] Matthew J. Rardin,[1] Defne Yarar,[4] Cheri S. Lazar,[1] Raffi Tonikian,[5] Antonius Koller,[2] Susan S. Taylor,[2] Charles Boone,[5] Sachdev S. Sidhu,[6] Sandra L. Schmid,[4] Gail A. Hecht,[3] and Jack E. Dixon[1,2]

[1]Departments of Pharmacology, Cellular and Molecular Medicine, and Chemistry and Biochemistry and [2]The Howard Hughes Medical Institute, University of California, San Diego, La Jolla, CA 92093
[3]Department of Medicine, Section of Digestive Diseases and Nutrition, University of Illinois at Chicago, Chicago, IL 60612
[4]Department of Cell Biology, The Scripps Research Institute, La Jolla, CA 92037
[5]Banting and Best Department of Medical Research and Department of Medical Genetics and Microbiology, University of Toronto, Toronto, Ontario M5S 3E1, Canada
[6]Department of Protein Engineering, Genentech Inc., South San Francisco, CA 94080

Bacterial toxins and effector proteins hijack eukaryotic enzymes that are spatially localized and display rapid signaling kinetics. However, the molecular mechanisms by which virulence factors engage highly dynamic substrates in the host cell environment are poorly understood. Here, we demonstrate that the *enteropathogenic Escherichia coli* (EPEC) type III effector protein EspF nucleates a multiprotein signaling complex composed of eukaryotic sorting nexin 9 (SNX9) and neuronal Wiskott-Aldrich syndrome protein (N-WASP). We demonstrate that a specific and high affinity association between EspF and SNX9 induces membrane remodeling in host cells. These membrane-remodeling events are directly coupled to N-WASP/Arp2/3–mediated actin nucleation. In addition to providing a biochemical mechanism of EspF function, we find that EspF dynamically localizes to membrane-trafficking organelles in a spatiotemporal pattern that correlates with SNX9 and N-WASP activity in living cells. Thus, our findings suggest that the EspF-dependent assembly of SNX9 and N-WASP represents a novel form of signaling mimicry used to promote EPEC pathogenesis and gastrointestinal disease.

Introduction

Virulence associated with several Gram-negative bacterial pathogens requires the translocation of "effector" proteins from bacteria into host cells through a dedicated protein translocation apparatus termed the type III secretion system (TTSS) (Galan and Collmer, 1999; Cornelis and Van Gijsegem, 2000). Many bacterial effector proteins possess a specialized activity required to limit anti-microbial immune response and promote bacterial growth and dissemination during pathogenesis. We are particularly interested in the mechanisms of type III effector proteins found in the attaching and effacing (A/E) pathogen group including *enteropathogenic Escherichia coli* (EPEC) and its close relatives, *enterohaemorrhagic Escherichia coli* (EHEC 0157:H7) and *Citrobacter rodentium* that cause severe gastrointestinal disease. Although the coordinated actions of several type III effector proteins including Tir, Map, EspF, EspG, EspH, EspI, EspJ, EspK, EspZ, and NleA-F are required for virulence associated with A/E pathogens, the biochemical activities of most effectors are poorly defined.

Microbial pathogens may hijack the actin cytoskeleton machinery to perform a variety of functions that include actin-based motility, cellular invasion, and intracellular trafficking through the endocytic pathway (Gruenheid and Finlay, 2003). A key regulator of the actin cytoskeleton is neuronal Wiskott-Aldrich syndrome protein (N-WASP), a eukaryotic protein that initiates actin filament branching and assembly through the direct activation of the Arp2/3 complex. Due to its critical role in this process, N-WASP is tightly regulated by upstream signals including phospholipids (PIP_2), the small G-protein Cdc42,

A.W. Weflen, M.J. Rardin, and D. Yarar contributed equally to this paper.

Correspondence to Jack E. Dixon: jedixon@ucsd.edu

N.M. Alto's present address is Department of Microbiology, University of Texas Southwestern Medical Center, S323 Harry Hines Blvd., Dallas, TX 75390-9048.

Abbreviations used in this paper: A/E, attaching and effacing; BAR, Bin/Amphiphysin/Rvs; CCP, clathrin-coated pit; CRIB, Cdc42/rac interactive binding; EHEC, *enterohaemorrhagic Escherichia coli*; EPEC, *enteropathogenic Escherichia coli;* N-WASP, neuronal Wiskott-Aldrich syndrome protein; PRR, proline-rich repeat; PX, phox; SH3, Src homology-3; SNX9, sorting nexin 9; TER, trans-epithelial electrical resistance; TTSS, type III secretion system.

The online version of this article contains supplemental material.

The Journal of Cell Biology, Vol. 178, No. 7, September 24, 2007 1265–1278
http://www.jcb.org/cgi/doi/10.1083/jcb.200705021

and Src homology-3 (SH3) adaptor proteins (Higgs and Pollard, 2001). Recent work also indicates that N-WASP is intimately associated with mechanisms of endocytosis (Merrifield et al., 2004; Benesch et al., 2005; Kaksonen et al., 2006), a cellular process required for the uptake of extracellular components including microbial pathogens and viruses (Veiga and Cossart, 2006).

Membrane remodeling during endocytosis requires the spatiotemporal coordination of several phospholipids and F-actin binding proteins (Merrifield et al., 2002; Kaksonen et al., 2005). As a specific example, sorting nexin 9 (SNX9) is dynamically recruited to clathrin-coated pits (CCPs) at the late stages of vesicle formation (Lundmark and Carlsson, 2003; Soulet et al., 2005). Although the exact role of SNX9 is not well understood, its domain architecture suggests that it links the plasma membrane to proteins associated with the cellular cortex. SNX9 possesses two lipid interaction domains, a phospholipid-binding module termed the phox (PX) domain followed by a putative Bin/Amphiphysin/Rvs (BAR) lipid-binding domain. Interestingly, the BAR domain is a banana-shaped helical dimer that senses membrane curvature and can reconfigure lipid vesicles or sheets into membrane tubules (Peter et al., 2004). In addition to its lipid-binding properties, SNX9 also possesses an N-terminal Src homology-3 (SH3) protein interaction module that was recently shown to bind WASP (Badour et al., 2007) and to functionally activate dynamin at CCPs (Soulet et al., 2005). Thus, SNX9 is uniquely suited to regulate the membrane/cytoskeletal interface during clathrin-mediated endocytosis.

In this paper, we found that the type III effector EspF coordinates membrane remodeling and F-actin polymerization during EPEC pathogenesis. Similar to previous results (Marches et al., 2006), we found that EspF binds the SH3 domain of SNX9 and we further demonstrated that this interaction induces membrane remodeling, a phenotype that is functionally coupled to N-WASP–dependent actin polymerization in eukaryotic cells. EspF activated both SNX9 and N-WASP in a coordinated spatiotemporal pattern at CCPs. Importantly, these data provide a molecular mechanism for EspF function in host cells and further suggest that the dynamic interplay between bacterial type III effector proteins and eukaryotic signaling pathways is a critical aspect of host–pathogen interactions.

Results

Identification of SNX9 and N-WASP as an EspF-binding protein

Database searches reveal that EspF orthologues are found in an A/E pathogen group that includes EPEC, EHEC 0157:H7, and *Citrobacter rodentium* (Fig. 1, A and B). EspF is composed of

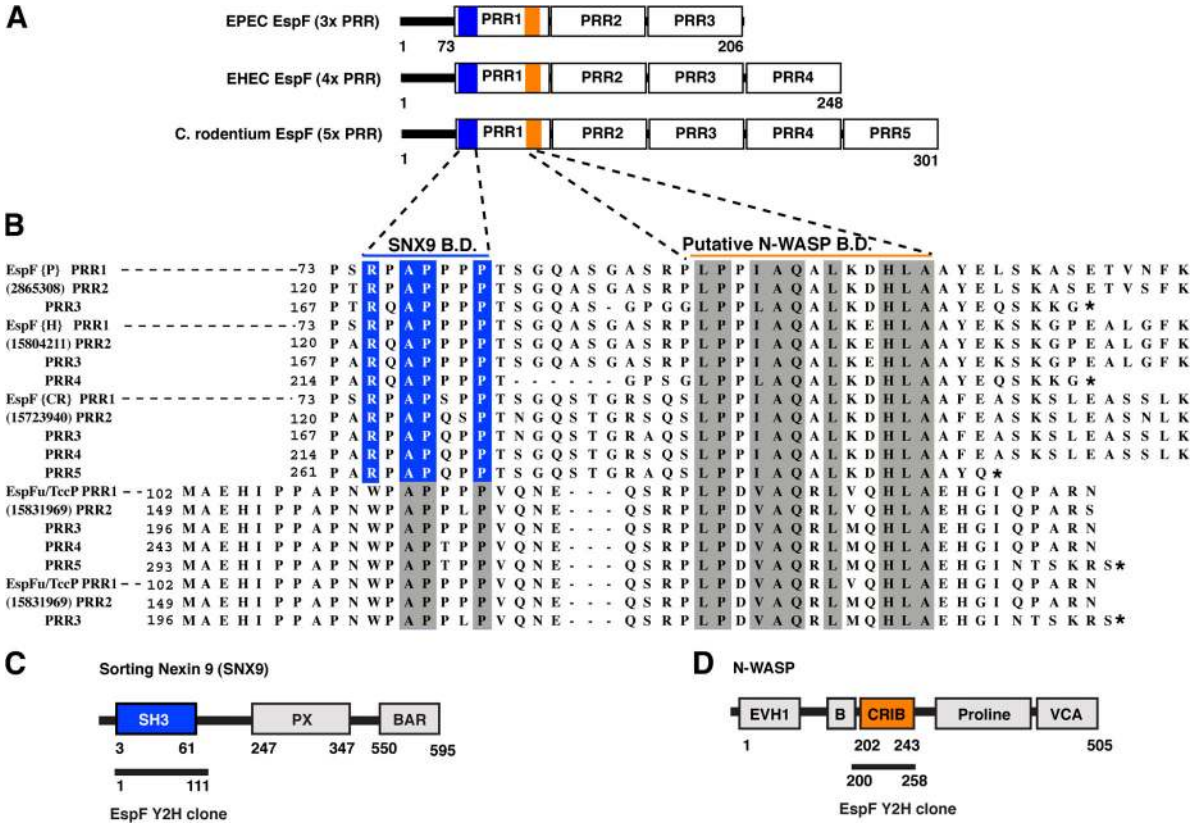

Figure 1. **The EPEC effector EspF binds both SNX9 and N-WASP.** (A) Schematic of EspF proline-rich repeat (PRR) domains from EPEC, EHEC 0157:H7, and *Citrobacter rodentium*. SNX9 (blue) and putative N-WASP (orange) binding sites are shown. (B) Clustal alignment comparing each PRR domains of EspF from EPEC (EP), EHEC 0157:H7 (EH), and *Citrobacter rodentium* (CR) to those of EspFu/TccP (EH). GenBank accession no. is listed. The SNX9 binding site is highlighted in blue; and putative N-WASP binding residues are shown in orange. (C) Schematic of SNX9 showing the Src homology-3 (SH3), p47 oxidase (PHOX), and Bin-Amphiphysin-RVS (BAR) domains. The cDNA clone (residues 1–111) that interacts with EspF is indicated. (D) Schematic of N-WASP showing the Enabled/VASP homology 1 (EVH1), the Cdc42/rac interactive binding (CRIB), the poly-proline (Proline), and the Verpolin/Cofilin/Acidic (VCA) domain. The cDNA clone (residues 200–258) that interacts with EspF is indicated.

47 amino acid proline-rich repeats (PRRs) that are repeated several times throughout the coding sequence. Although the repeat numbers vary amongst EspF orthologues in A/E pathogens, there are no cases where the PRR sequence is present as a single copy. In addition, EHEC 0157:H7 possesses a second PRR domain protein called EspFu/TccP that shares 35% homology with EspF, but has a distinct biological function (Campellone et al., 2004; Garmendia et al., 2004). To define eukaryotic binding partners we screened EspF against a mouse embryo cDNA library using the yeast two-hybrid system. Screening of 8 million yeast transformants yielded five positives. Two cDNAs encoded the SH3 domain of SNX9 (Fig. 1 C, residues 1–111) and the Cdc42/rac interactive binding (CRIB) domain of N-WASP (Fig. 1 D, residues 200–258).

EspF binds SNX9 through a highly evolved SH3 ligand motif

Our yeast two-hybrid clone spanned residues 1–111 of SNX9, a region encompassing its SH3 domain. This interaction was confirmed using [^{35}S]-methionine labeled SNX9 1–111 (SH3 domain) and recombinant GST-EspF fusion protein, which selectively interacted in pull-down assays (Fig. 2 A). Grb2, Nck1, and Nck2, three SH3 domain–containing proteins with broad ligand specificity, could not be copurified with EspF (Fig. 2 A). Similar binding specificity was also observed in vivo by co-immunoprecipitation assays from transfected Hek293A cells. These data demonstrate that EspF interacts with full-length SNX9 but not Grb2, Nck1, or Nck2 in cells (Fig. 2 B).

In general the ~300 SH3 domains in the human genome bind ligands with a canonical PxxP motif. It was surprising that only one SH3 protein was identified in our high coverage yeast two-hybrid screen. To better understand this apparent specificity, we used phage-displayed peptide libraries to explore the binding specificity profiles of the SH3 domain of SNX9. The SH3 domain was screened against a library composed of 10^{10} completely random dodecapeptides. After four rounds of affinity selection, 150 individual binding-phage were sequenced. Remarkably, only 13 unique peptides were identified from the 150 sequences, suggesting that SNX9 recognizes a highly conserved sequence motif (Fig. 2 C). Homology alignment was used to derive a SNX9 specificity profile in the form of a preferred binding motif (Fig. 2 C). Notably, the specificity profile confirmed that the SH3 domain recognizes multiple features of the ligand sequence; an arginine was invariant at the −3 position, alanine was preferred at the −1, and prolines were selected at the 0 and +3 positions of the PxxP motif. These data determine the preferred consensus SNX9 SH3 ligand motif as RxAPxxP.

Next, an in vitro–translated ^{35}S-SNX9 was used to screen a solid phase library containing peptides of 15-mer residues (offset every three residues) spanning amino acids 1–166 in EspF (Fig. 2 D). By overlaying ^{35}S-SNX9 onto the EspF peptide library, we found that the SH3 binding site in EspF was confined

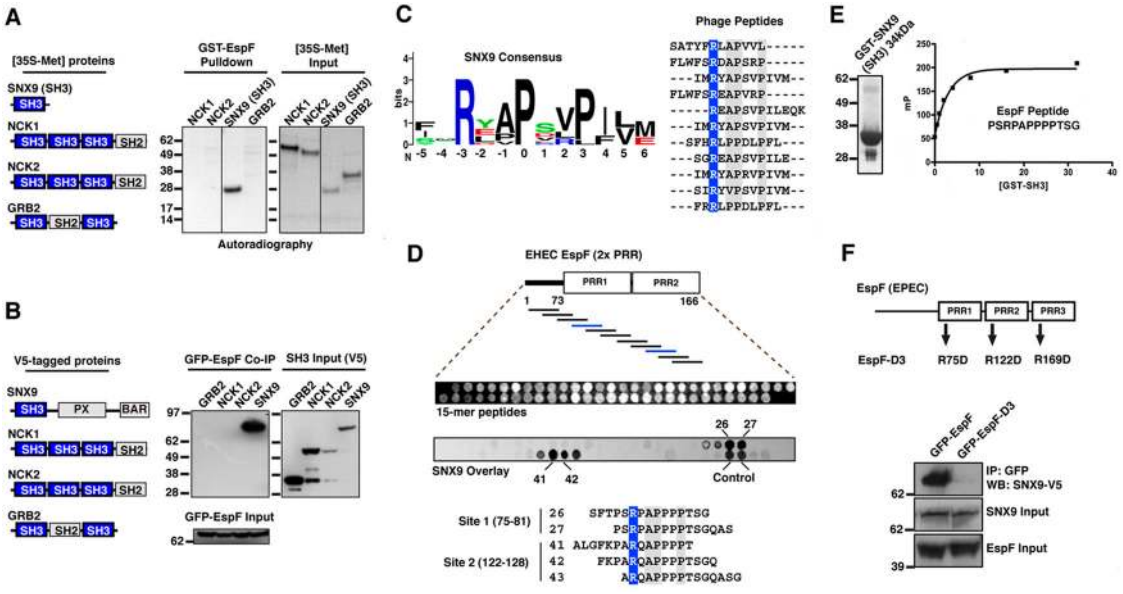

Figure 2. **Identification of motifs required for direct EspF and SNX9 interactions.** (A) Glutathione-Sepharose pull-down with 10 μg of GST-EspF (residues 48–206) mixed with the [^{35}S]-methionine proteins indicated (left diagram). Autoradiograph of GST pulldown (left) and of 1/20th input of ^{35}S-labeled NCK1, NCK2, SNX9 (residues 1–111), and GRB2 is shown (right). (B) HEK293A cells were cotransfected with EGFP-EspF and V5-tagged proteins indicated (left diagram). Anti-GFP immunoprecipitations (IP) were probed by V5 immunoblot (IB) (left). Cell lysates were probed by V5 or GFP immunoblot to show input levels. (C) Logos plot of the SNX9 binding consensus sequence derived by phage display experiments (left). Alignment of 13 unique SNX9 binding sequences used to derive the consensus is shown. The invariant arginine (blue) and highly conserved residues (gray) are highlighted. (D) Peptide array analysis of the SNX9-binding sites on EspF. Top: diagram of EspF residues 1–166 used for the peptide scanning experiments. Middle: ultraviolet (UV) illumination shows the qualitative amount of each peptide synthesized (top). Bottom: solid-phase binding of ^{35}S-SNX9 to 15-mer EspF peptides was assessed by autoradiography. An alignment of EspF-binding peptides from two SNX9 binding series is shown. (E) Saturation binding curves were generated with increasing concentrations of GST-SNX9-SH3 (left) to a fixed concentration of EspF peptide by fluorescence polarization (see Materials and methods). (F) HEK293A cells were cotransfected with EGFP-EspF or triple mutant EGFP-EspF-D3 (top diagram) and V5-tagged SNX9. Anti-GFP immunoprecipitations (IP) were probed by V5 immunoblot (IB) (top panel). Cell lysates were probed by V5 or GFP immunoblot to show input levels (bottom two panels).

to two distinct regions within residues 75–81 and 122–128 (Fig. 2 D). Remarkably, these regions in EspF both possess a common RxAPxxP motif that conforms to the SNX9 SH3 consensus-binding motif identified in our unbiased phage display. Because residues 75–81 and 122–128 are found at the N-terminal portion of PRR domain 1 and 2, respectively, and because homologous regions are found in all EspF orthologues, we can conclude that each PRR domain of EspF possesses a single SNX9 binding site (see the alignment in Fig. 1). In support of this conclusion, a dissociation constant of 2.2 μM was experimentally derived from an EspF peptide (RPAPPPP) bound to the SNX9-SH3 domain (Fig. 2 E), suggesting that these residues constitute the minimal sequence required for SNX9 interaction. In addition, we substituted aspartic acids for the arginines in position 75, 122, and 169 ($Arg^{75,122,169}$→Asp or EspF-D3) in all three PRR domains of EPEC EspF. Mutant EspF-D3 failed to bind SNX9 in both in vitro pull-down assays (unpublished data) and coimmunoprecipitation experiments (Fig. 2 F).

EspF induces Arp2/3-dependent actin assembly through the direct activation of N-WASP

Next, we turned to the interaction between EspF and N-WASP. Full-length N-WASP interacted with EspF in coimmunoprecipitation assays, but not with control EGFP (Fig. 3 A). This interaction was comparable to the interaction between N-WASP and prophage-expressed EspFU/TccP gene that displays 35% identity to EspF (Fig. 1 B) (Garmendia et al., 2006). These data suggest that the functionally distinct EspF and EspFU/TccP proteins both interact with N-WASP in eukaryotic cells.

We tested the ability of EspF to directly activate N-WASP by assaying Arp2/3 complex-dependent actin polymerization kinetics using a pyrene-actin assembly assay in vitro. For these assays, we used Arp2/3-complex purified from bovine brain extracts and purified N-WASP ΔEVH1 (residues 138–501), an N-WASP truncation mutant lacking the WH1/EVH1 domain that exhibits strong autoinhibition (Fig. 3 B) (Co et al., 2007). In addition, a purified 6×-His tagged EspF protein possessing three intact PRR domains was used in these studies (EspFΔ47, residues 48–206) (Fig. 3 B). In the absence of either N-WASP or the Arp2/3 complex, EspF did not alter F-actin assembly dynamics (Fig. 3 C). However, in the presence of both Arp2/3 and N-WASP ΔEVH1, EspF stimulated actin nucleation (Fig. 3 C). These data indicate that EspF directly activates N-WASP in vitro.

As demonstrated in Fig. 1 D, residues 200–258 encompassing the Cdc42 binding CRIB domain of N-WASP constituted the minimal interaction site with EspF, suggesting that EspF could functionally mimic this GTPase. We used an engineered "mini N-WASP" protein possessing the minimal Basic and CRIB regulatory domains linked to the Arp2/3 activating VCA domain to test this hypothesis (Fig. 3 B) (Prehoda et al., 2000). EspF potently stimulated mini-N-WASP in a dose-dependent manner and the half-maximal activity of mini-N-WASP occurred at an EspF concentration of 11.8 nM as determined by saturation binding experiments (Fig. 3 C). In total, these data indicate that EspF can relieve N-WASP autoinhibition through a direct binding interaction with the CRIB regulatory domain.

EspF nucleates an active complex composed of SNX9 and N-WASP in vitro

Because both N-WASP and SNX9 bind to residues within the PRR domains of EspF, it was important to determine if their binding sites were mutually exclusive. We found that the SNX9 binding deficient mutant EspF-D3 induced mini-N-WASP–dependent actin polymerization to a similar extent as EspF, suggesting that the RxAPxxP motif did not play a role in N-WASP activation (Fig. 3 E). Moreover, addition of saturating concentrations of GST-SNX9-SH3 (10 μM) to EspF had a minor affect on N-WASP activation (Fig. 3 E), suggesting the possibility that EspF can bind SNX9 and N-WASP through two distinct interaction sites.

To directly test the ability of EspF to nucleate a functional SNX9 and N-WASP complex, we first incubated recombinant EspF with GST-SNX9-SH3 immobilized to glutathione-Sepharose beads (Fig. 3 F). The formation of a stable protein complex between the SH3 domain (34 kD) and EspF (26 kD) was confirmed by SDS-PAGE analysis (Fig. 3 F). Next, we added the stable SH3/EspF complex to mini-N-WASP and measured actin polymerization rates (Fig. 3 G). The SH3/EspF complex directly activated mini-N-WASP–mediated actin assembly kinetics (Fig. 3 G, blue). In control experiments, actin polymerization kinetics were not increased with SH3 beads alone (Fig. 3 G, gray), with mutant EspF-D3 that could not form a complex with the SH3 beads (Fig. 3 G, purple), or with GST control proteins (Fig. 3 G, black). In total, these data provide strong evidence that EspF coordinates the binding of SNX9 and the activation of N-WASP through two independent binding motifs found within its highly conserved PRR domains (see Fig. 1 B).

EspF dynamics observed in living cells

SNX9 and N-WASP participate in several membrane trafficking events and localize to cellular membranes at CCPs and trafficking organelles (Merrifield et al., 2002, 2005; Benesch et al., 2005; Soulet et al., 2005; Yarar et al., 2005). We used total internal reflection-fluorescence microscopy (TIR-FM), a technique that allows fluorophore-conjugated proteins to be visualized within 100 nm of the cell surface (Steyer and Almers, 2001), to determine if EspF also localized to the plasma membrane in living cells. EGFP-EspF was transfected into Swiss-3T3 cells stably expressing DsRed-Clathrin light chain- a (Clc-DsRed), a cellular marker of CCPs and the plasma membrane (Merrifield et al., 2002). Several 10–12-min videos were recorded in which EGFP-EspF and Clc-DsRed fluorescence was simultaneously captured by dual-color TIR-FM (Video 1, available at http://www.jcb.org/cgi/content/full/jcb.200705021/DC1).

Analysis of living cells indicated that EspF was highly dynamic at the plasma membrane and it transiently accumulated into patches at the cell surface (Video 1). Interestingly, EspF partially colocalized with clathrin in still images (Fig. 4 A) and examination of time-resolved videos indicated that 92% (357 of 388 events from 8 cells) of clathrin structures transiently colocalized with EspF (Fig. 4 B and Video 2, available at http://www.jcb.org/cgi/content/full/jcb.200705021/DC1). In addition, larger EspF tubules could be found extending near the cell surface (Video 3). Expression of EspF did not affect normal clathrin dynamics, as the

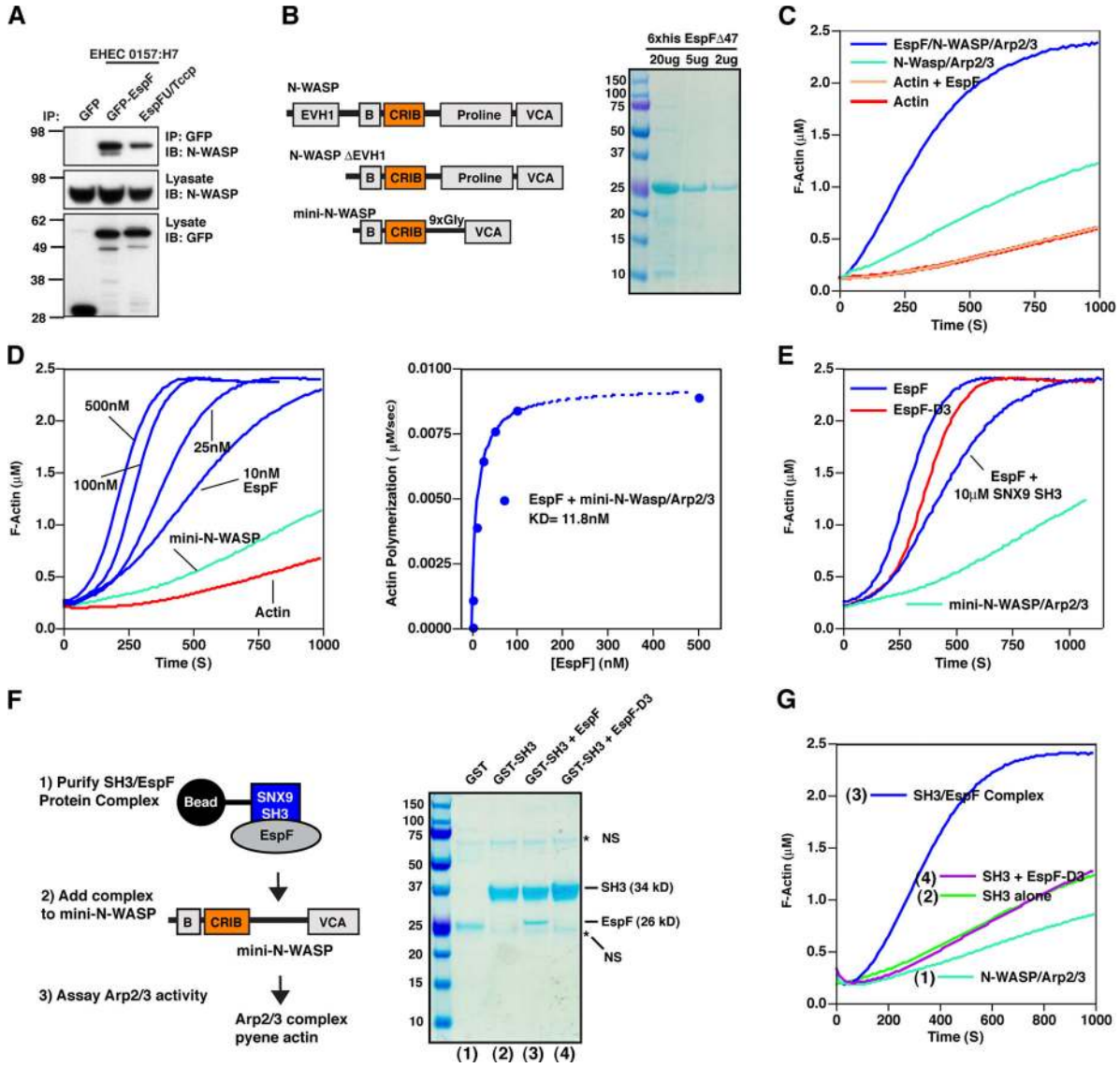

Figure 3. **EspF directly binds to and activates N-WASP.** (A) HEK293A cells were cotransfected with EGFP-EspF, EGFP-EspFu/TccP, or control EGFP and V5-tagged N-WASP. Anti-GFP immunoprecipitations (IP) were probed by V5 immunoblot (IB) (top). Cell lysates were probed by V5 or GFP immunoblot to show input levels (bottom two panels). (B) A diagram depicting N-WASP ΔEVH1 and mini-N-WASP proteins used in actin polymerization experiments and a Coomassie-stained gel of purified 6×His EspFΔ47 (residues 48–206) used in the actin polymerization experiments. (C) Pyrene-actin assembly assay demonstrating EspF activates N-WASP in vitro. The polymerization kinetics of actin alone (red) was not increased by addition of 500 nM EspF (gold). Polymerization curves of Arp2/3 and N-WASPΔEVH1 (light green) compared with these components plus 500 nM EspF (blue) is shown. Unless otherwise stated, all assays contain 2.5 μM pyrene-actin, 40 nM Arp2/3 complex, and 100 nM N-WASP proteins. (D) EspF activates mini-N-WASP in vitro. A pyrene-actin assembly assay showing that EspF activated mini-N-WASP in a dose-dependent manner (blue). The rate of actin polymerization for each EspF concentration was determined at 2 μM G-actin consumption (80%) and plotted against EspF protein concentration (right graph). (E) Pyrene actin assembly assays comparing EspF (100 nM) and mutant EspF-D3 (100 nM) activating mini-N-WASP. Addition of 10 μM GST-SNX9 (SH3) domain to EspFΔ47 had a negligible affect on mini-N-WASP activation. (F) Schematic depicting the experimental procedure for Fig. 3 G (left) and an SDS-PAGE of GST (1), GST-SNX9-SH3 (2), GST-SNX9-SH3 in complex with EspFΔ47 (3), and GST-SNX9-SH3 control that did not form a complex with mutant EspF-D3 (4). The mobility of the stable SH3/EspFΔ47 complex is indicated. Non-specific (NS) bands are indicated (*). (G) Mini-N-WASP actin polymerization assay on protein complexes described in Fig. 3 F.

lifetime of clathrin at the plasma membrane was nearly identical between untransfected cells (62 ± 4 s, $n = 60$ events) and EGFP-EspF transfected cells (64 ± 5 s, $n = 58$ events) (Fig. 4 C). These dynamics were similar to those previously reported for clathrin in Swiss 3T3 cells (Merrifield et al., 2002).

We noticed that the spatial and temporal dynamics of EspF were exquisitely coordinated with clathrin-mediated endocytic events. To quantify these observations, the surface kinetics of EspF was directly compared with clathrin dynamics. As a reference index, the Clc-DsRed fluorescence intensity values of 25 clathrin structures were measured from 8 cells expressing EGFP-EspF. We analyzed events in which clathrin appeared at the plasma membrane, was stable for ~60 s in the TIR-FM imaging field, and exponentially decayed from the plasma membrane (Fig. 4 D, red trace). These measurements were directly compared with the EGFP-EspF fluorescence intensities at each CCP. By aligning all 25 EspF traces relative to clathrin membrane departure, it was clear that EspF displayed a tightly

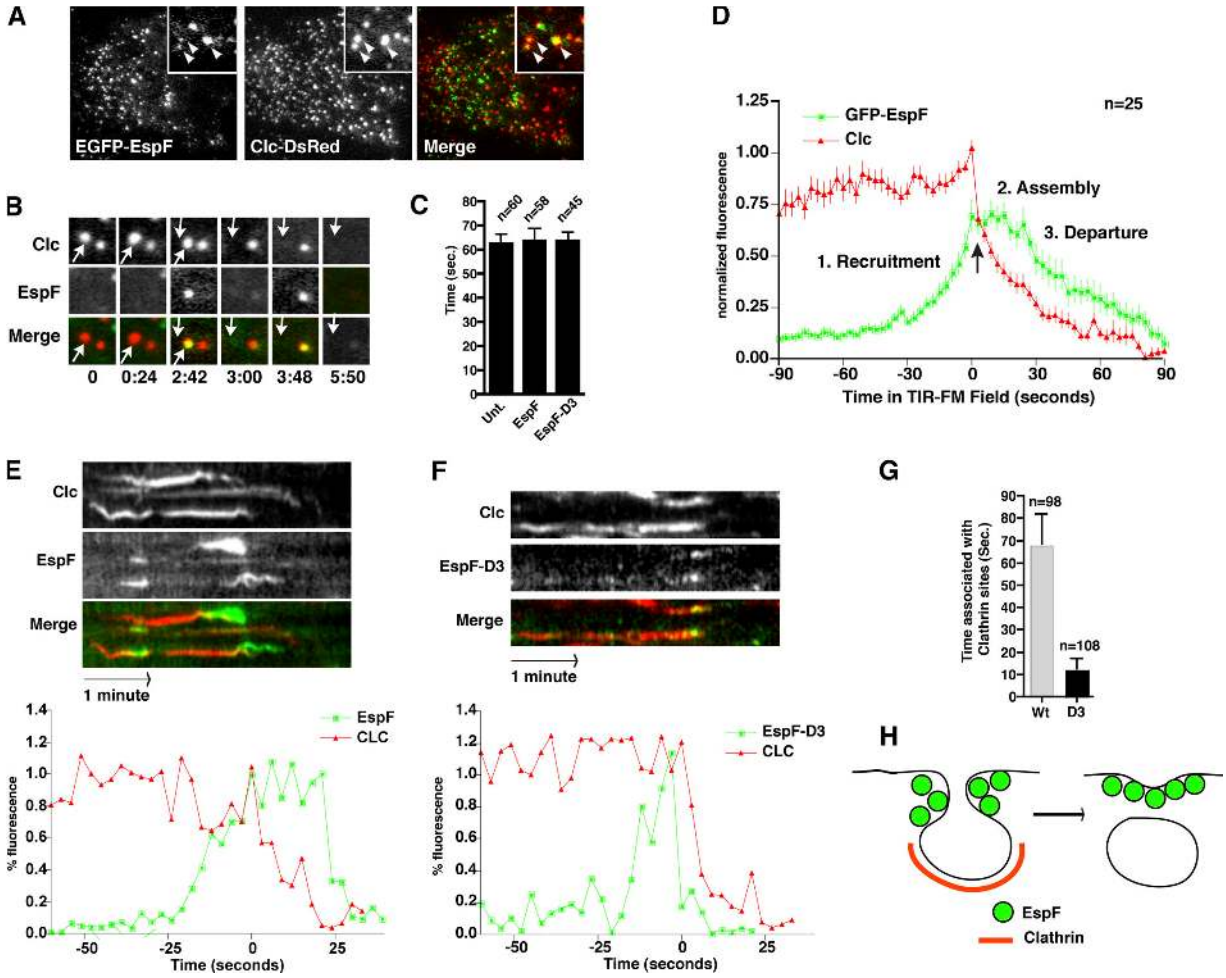

Figure 4. **EspF transiently associates with clathrin at endocytic sites.** (A) Dual-color TIR-FM image of cells expressing EGFP-EspF and Clc-DsRed and merged image showing partial colocalization. (B) Time series of two stereotypical EspF puncta correlated with simultaneous Clc-DsRed dynamics using live cell TIR-FM. Arrows track a single clathrin endocytic event. (C) The cell surface lifetimes of Clc-DsRed in untransfected, EGFP-EspF, and EGFP-EspF-D3 transfected Swiss-3T3 cells. The average lifetime and SEM of CCPs from at least five cells are shown. (D) Average fluorescence traces of Clc-DsRed (red) or EGFP-EspF (green) from 25 individual CCPs. Arrow indicates the time of peak EGFP-EspF signal at the moment of clathrin departure. SEM of averaged traces is shown. Time points represent (1) the recruitment of EspF, (2) the assembly phase of EspF at the plasma membrane, and (3) the departure of EspF. (E and F) Analysis of individual EGFP-EspF (E) or EGFP-EspF-D3 (F) puncta by TIR-FM. Top: kymograph representation of single CCPs. Bottom: representative fluorescence trace of single CCPs as described in D. (G) The cell surface lifetimes of EGFP-EspF or mutant EspF-D3 associated with endocytic sites are shown. The average lifetime and SEM of ~100 CCPs events from at least five cells and three separate experiments are shown. (H) Diagram depicting EspF associated with highly curved membranes at single CCPs.

coordinated spatiotemporal localization pattern at the plasma membrane. First, EspF was recruited to the plasma membrane at preexisting CCPs (Fig. 4 D, green trace). The peak EspF fluorescence signal coincided with the exponential decay of clathrin signal from the plasma membrane (Fig. 4 D, arrow). Because these clathrin dynamics are indicative of clathrin coated-vesicle movement away from the plasma membrane and vesicle scission (Merrifield et al., 2005), EspF is likely to associate with actively budding membrane domains. Second, EspF remained at the cell surface beyond the time of clathrin departure, suggesting that EspF was associated with the plasma membrane and not in CCPs (Fig. 4 D). Finally, EspF signal decayed in the TIR-FM image, indicating its retreat from the plasma membrane.

Next, we examined if EspF dynamics at the plasma membrane correlated with the protein interactions defined by our in vitro data. The triple-mutant EspF-D3 protein did not interact with SNX9, but maintained N-WASP binding activity (Fig. 2 F and Fig. 3 E). Therefore, this mutant was used to determine the potential contributions of SNX9 binding on EspF dynamics. We recorded several TIR-FM videos from cells expressing EGFP-EspF-D3 (Fig. 4 E) and compared its dynamics to wild-type EspF (Fig. 4 F). EspF-D3 was recruited to 86% (112 of 130 events from 5 cells) of cell surface clathrin structures. Unlike EspF, however, EspF-D3 departed from the plasma membrane coincident with or slightly before clathrin-mediated endocytosis (Fig. 4 F). The average lifetime of EspF-D3 associated with endocytic sites (12.3 ± 5 s, n = 108 events) was approximately fivefold shorter than wild-type EspF (68 ± 14.5 s, n = 98 events) (Fig. 4 G). It was also clear that EspF-D3 did not exhibit the prolonged plasma membrane localization that wild-type EspF displayed after clathrin departure. These data are consistent with the ability of EspF to interact with SNX9 at the plasma membrane (Fig. 4 H); however, additional experimental approaches are necessary to directly establish this link.

EspF remodels cellular membranes through the activation of SNX9

Using wide-field fluorescence microscopy, we found that endogenous SNX9 localized to CCPs at the surface of HeLa cells and accumulated in perinuclear regions near the Golgi apparatus (Fig. 5 A) (Lundmark and Carlsson, 2003; Soulet et al., 2005). Transient transfection of EspF induced a redistribution of SNX9 from CCPs and perinuclear regions to "worm-like" tubular structures found near the cell periphery (Fig. 5 A; Fig. S1 A, available at http://www.jcb.org/cgi/content/full/jcb.200705021/DC1). In these cells SNX9 and EspF colocalized at tubular structures, suggesting that SNX9 redistribution was directly associated with EspF binding (Fig. 5 A and Fig. S1 B). Consistent with this notion, mutant EspF-D3 had no affect on SNX9 localization. To test these observations in a more controlled cellular environment, we artificially increased the SNX9 expression levels by transfecting mCherry-SNX9 into HeLa cells. Exogenous SNX9 had a predominantly perinuclear localization and a small proportion could also be found in cell surface puncta reminiscent of CCPs (Fig. 5 B). We found that coexpression of EspF with SNX9 induced an array of tubular structures that extended into dense tubular networks (Fig. 5 B). Similar tubular networks were identified in >90% of EspF and SNX9 cotransfected cells and both proteins colocalized at these sites (Fig. 5, B and C). As expected, mutant EspF-D3 failed to induce SNX9 tubules indicating that SH3 binding is required for SNX9 localization. Moreover, wild-type EspF did not induce tubules upon cotransfection of SNX9ΔBAR, a C-terminal deletion mutant of SNX9 in which the putative membrane deforming BAR domain was removed (Fig. 5, B and C). These data reveal a novel activity of SNX9 to induce cellular tubulation, a phenomenon that is directly linked to EspF binding.

To determine the nature of the abnormal tubules formed by coexpression of EspF and SNX9, EspF was first immunolocalized by electron microscopy (EM). EspF decorated tubular and vesicular membrane structures but was not found in nuclear areas, inside organelles, or randomly distributed throughout the cytoplasm (Fig. 5 D). Using thin-section EM we identified a striking array of membrane structures in EspF transfected (Fig. 5 E) but not untransfected cells (Fig. 5 F). The EspF-induced tubules were abnormally curved and in many cases budding profiles could be observed along both sides of the membrane tubules (Fig. 5 G). In addition, unusually long (~0.5 μm) cell surface invaginations appeared to be continuous with the plasma membrane (Fig. 5 H) and several membrane projections extended from multivesicular organelles (Fig. 5 I). A dense negative stain was also observed around the new membrane structures, most likely representing the EspF/SNX9 protein coat. We now propose a model whereby EspF activates SNX9; engagement of the SNX9-SH3 domain by the highly specific EspF-ligand motif exposes the C-terminal BAR domain to induce membrane remodeling in eukaryotic cells.

EspF coordinates membrane remodeling and actin polymerization in cells

N-WASP was originally shown to induce cell surface filopodia projections during cell migration (Miki et al., 1998); however, recent findings indicate that it also regulates membrane trafficking events including actin-based vesicular transport and endocytosis (Merrifield et al., 2002, 2004; Benesch et al., 2005; Innocenti et al., 2005; Yarar et al., 2005). We did not detect the formation of cell surface filopodia in EspF-transfected cells. However, de novo F-actin nucleation occurred near membrane tubules induced by EspF and SNX9 coexpression (Fig. 6 A; Fig. S2 A, available at http://www.jcb.org/cgi/content/full/jcb.200705021/DC1). EspF activation of SNX9 was prerequisite for these downstream signaling events, as F-actin appeared normal in cells expressing mutant EspF-D3 (Fig. 6 B). These data suggest that membrane tubulation occurs before actin polymerization in the EspF/SNX9/N-WASP signaling cascade. In support of this conclusion, depolymerization of actin had no affect on the formation of membrane tubules; however F-actin was perturbed at these sites (Fig. S2, C and D). Moreover, N-WASP redistributed from the cellular cytoplasm to membrane tubules in EspF-transfected cells (Fig. 6 C) but not in cells expressing mutant EspF-D3 (Fig. 6 D). In total, these data indicate that membrane targeting and subsequent remodeling by EspF is required for its activation of downstream signaling events.

Several additional lines of evidence also suggest that EspF activates N-WASP at membrane sites. Careful examination of the cell surface dynamics of EspF by TIR-FM indicated that a small proportion of EspF puncta (~5%) formed "comet tails" and seemed to propel the clathrin structure over a very short distance just before clathrin internalization (Fig. 6 E; Video 4, available at http://www.jcb.org/cgi/content/full/jcb.200705021/DC1). This EspF behavior is reminiscent of actin filament dynamics observed in *Listeria* comet tails (Theriot et al., 1992) and the projectile motion of endocytic vesicles at the tips of actin tails (Merrifield et al., 1999). EspF was also found at mobile clathrin structures that moved parallel to the plasma membrane, a phenotype that may occur due to changes in the actin cytoskeletal architecture (Fig. 6 F; Video 5) (Yarar et al., 2005). In total, these cellular observations indicate that EspF functions as a bacterial signaling node, integrating the activation of two signaling cascades at membranes of eukaryotic cells (Fig. 6 G).

Investigation of bacterial delivered EspF in polarized epithelial cells

Next, we sought to determine the potential role of EspF signaling in epithelial models of EPEC infection. Genetic studies have implicated EspF in several pathogenic phenotypes, including the deregulation of the tight-junction ion barrier function in EPEC-infected polarized epithelial cells (McNamara et al., 2001; Dean and Kenny, 2004; Shifflett et al., 2005). We found a dramatic loss of trans-epithelial electrical resistance (TER, a measure of tight junction integrity) in polarized T84 colonic epithelial cells infected with wild-type EPEC that was dependent on the *espF* gene (Fig. 7 A) (McNamara et al., 2001). Interestingly, both plasmid-expressed EPEC *espF* (p*espF*) as well as EHEC *espFu/tccp* (p*espFu/tccp*) trans-complemented the *espF*$^-$ mutant strain (Fig. 7 A) (Viswanathan et al., 2004). Similarly, we found that *espF*$^-$ mutant strain expressing the SNX9 binding–deficient mutant EspF-D3 (*pespF-D3*) also induced a loss of TER (Fig. 7 A). These confounding data suggest that multiple

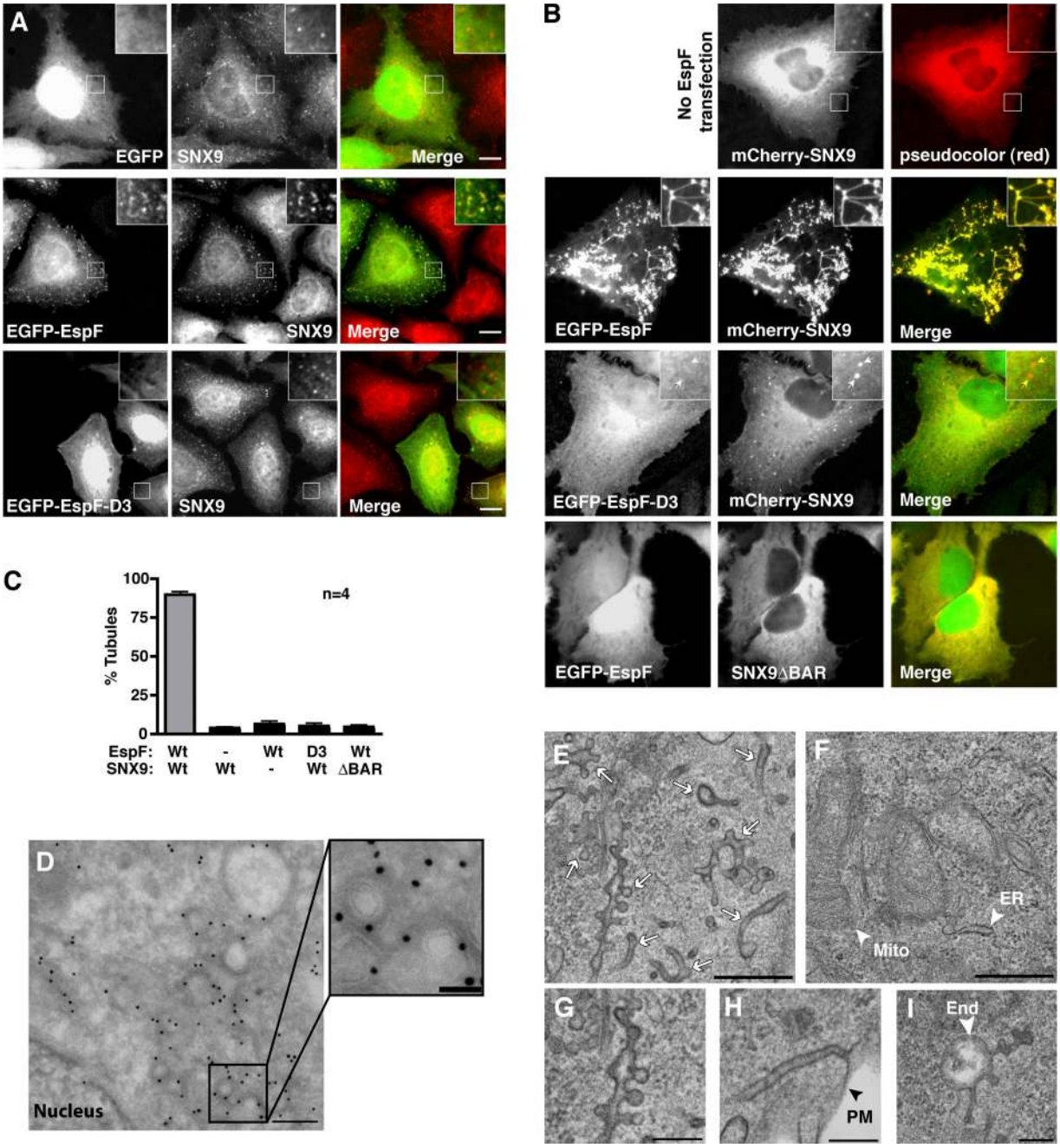

Figure 5. **EspF activates SNX9 to form membrane tubules in vivo.** (A) Fluorescence microscopy of endogenous SNX9 from EGFP, EGFP-EspF, or EGFP-EspF-D3 transfected HeLa cells. Inset shows the accumulation of SNX9 at CCPs or new tubule structures. Bar = 15 μm. (B) Fluorescence microscopy of HeLa cells transfected with mCherry-SNX9 or the EGFP constructs and mCherry-SNX9 as indicated. Inset shows CCPs (arrows) or new tubule structures. Bar = 15 μm. (C) Quantification of tubule networks in HeLa cells cotransfected with the indicated plasmids. Graphs represent the percentage of transfected cells with tubule networks from at least three independent experiments and SEM is shown. Wild-type (Wt), mutant EspF-D3 (D3), and SNX9ΔBAR (ΔBAR) are indicated. (D) Immunoelectron micrograph of EGFP-EspF in HeLa cells cotransfected with mCherry-SNX9. Sections were labeled with anti-GFP polyclonal antibody and 10 nm protein A-gold. Bars for large image (250 nm) and magnification (50 nm) are indicated. (E–I) Thin-section electron micrograph of EspF- and SNX9-transfected HeLa cells containing multiple membrane tubules showing irregular shapes (arrows) (E). Untransfected controls (F) and representative examples of unusual membrane tubules in EspF transfected cells are shown (G–I). Bars: 500 nm (E and F), 200 nm (G–I).

genes in EPEC are responsible for tight junction breakdown and suggest that the complex phenotype cannot be ascribed to EspF function alone.

Next, we wanted to directly test the cytoplasmic role of EspF in polarized epithelial cells. Tight junction breakdown was monitored by the redistribution of occludin from a uniform band outlining the cell junctions in uninfected cells (Fig. 7 B) to a discontinuous beaded pattern in EPEC infected cells (Fig. 7 C). To directly test the role of EspF in this process, stable cell lines expressing a tandem affinity protein tag (TAP; protein A and flag) fused to the N-terminus of EPEC EspF were created (Fig. 7 D). As shown in Fig. 7 E, TAP-EspF was expressed in

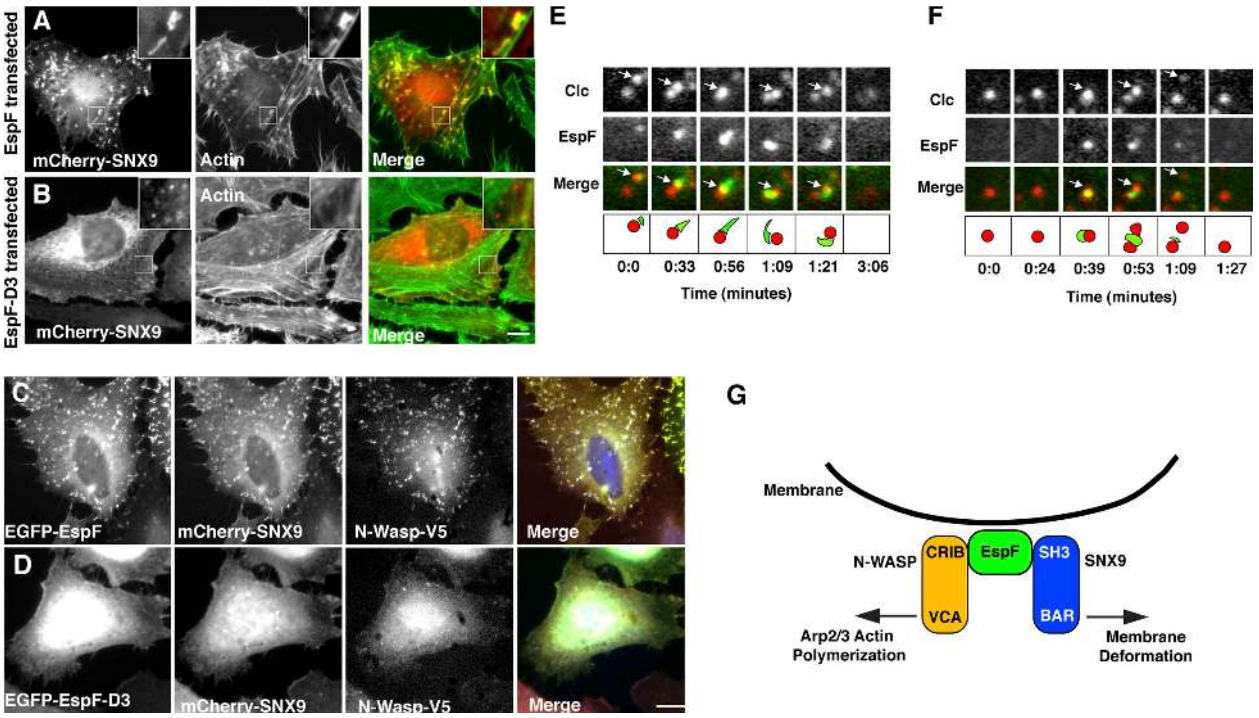

Figure 6. **EspF induces N-WASP activation at membrane tubules.** (A and B) Fluorescence microscopy images depicting mCherry-SNX9 and FITC-phalloidin (actin) in EspF (A) or EspF-D3 (B) transfected HeLa cells. Bar = 15 μm. (C and D) Fluorescence microscopy images of HeLa cells cotransfected with EGFP-EspF (C) or EGFP-EspF-D3 (D) with mCherry-SNX9 and N-WASP-V5. N-WASP was detected by anti-V5 immunocytochemistry. Bar = 15 μm. (E) Time series of EspF puncta (EGFP-EspF) exhibiting a "rocketing" phenotype (arrow) from live cell TIR-FM. Cartoon below. (F) Time series of EspF puncta (EGFP-EspF) exhibiting a mobile phenotype from live cell TIR-FM. Images are correlated with simultaneous Clc-DsRed dynamics showing the movement of a single CCP (arrow). (G) Schematic of EspF functioning as a node of signaling integration at eukaryotic membranes.

every cell and localized to small puncta near the apical cell surface. SNX9 interaction seemed to be required for this localization as the SH3-binding mutant EspF-D3 was distributed throughout the cytoplasm and accumulated in nuclear regions (Fig. 7 F). Importantly, MDCK cells expressing either EspF or EspF-D3 formed normal tight junctions (Fig. 7, E and F), suggesting that EspF activity alone is not sufficient to break down tight junctions. Next, we biochemically purified EspF from MDCK cells as an unbiased approach to determine protein complexes associated with EspF in a polarized cell type (Fig. 7 G). TAP-purified EspF or control parental cell lines were separated by SDS-PAGE and Coomassie stain indicated that the major EspF-binding protein had a molecular weight of ~70 kD (Fig. 7 G). This protein was unambiguously identified as canine SNX9 (MW = 71 kD) by tandem mass spectrometry from two independent experiments (see Materials and methods). Thus, SNX9 is the major target of cytoplasmic EspF in polarized epithelial cells.

Finally, we sought to determine if the localization and function of bacterial delivered EspF relies on interaction with SNX9 in polarized cell types. Human $CaCo_2$ intestinal epithelial cells were infected with wild-type EPEC or the *espF*$^-$ mutant strain. Whereas wild-type EPEC induced SNX9 membrane tubules, this phenotype did not occur in *espF*$^-$ mutant EPEC-infected cells (Fig. 7 H). The wild-type phenotype was rescued by introducing a plasmid encoding the *espF* allele (p*espF*) into the mutant *espF*$^-$ strain (Fig. 7 H). However, there was no phenotype associated with mutant strains complemented with SNX9 binding–deficient *espF-D3* (p*espF-D3*) (Fig. 7 H). Similar results were also found in EPEC-infected HeLa cells (unpublished data). Western blot analysis confirmed the expression and secretion of the EspF proteins by wild-type and trans-complemented strains (Fig. 7 I). These data further indicate that the biochemical activities of EspF that we have described in vitro are likely to occur during EPEC pathogenesis of intestinal epithelial cells.

Discussion

In this study we have obtained evidence for a new model of EspF function during bacterial pathogenesis. Our data suggest that EspF physically links membrane-trafficking proteins to the actin polymerization machinery in host cells. Several lines of evidence support this hypothesis. First, EspF interacts directly with SNX9 through a highly evolved SH3 domain–binding motif that is repeated several times throughout the EspF coding sequence. Second, EspF stimulates N-WASP/Arp2/3 actin polymerization in reconstitution experiments. Third, our live-cell imaging studies revealed that EspF dynamically localized to CCPs. This subcellular localization is similar to those previously described for both SNX9 and N-WASP (Merrifield et al., 2004; Benesch et al., 2005; Innocenti et al., 2005; Soulet et al., 2005). Fourth, EspF induced membrane remodeling through the activation of SNX9, and the actin polymerization profiles at these sites correlated with the ability of EspF to interact with N-WASP in cells. Finally, the EspF-dependent redistribution of SNX9 during bacterial infection suggests that the biochemical and cellular activities that we have described are likely to occur during natural EPEC pathogenesis.

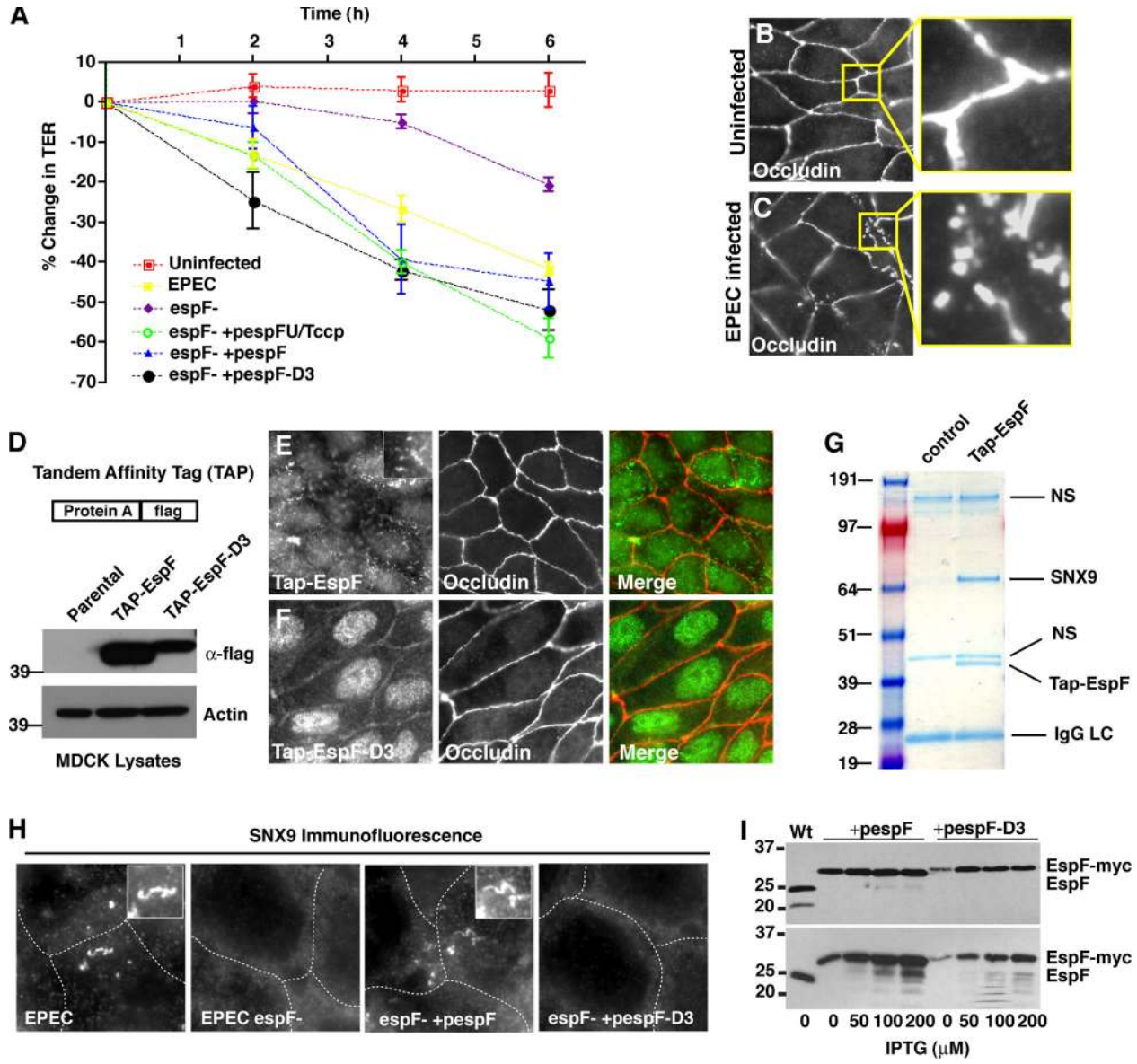

Figure 7. **SNX9 is the major binding partner for EspF in polarized epithelial cells.** (A) TER measurements of polarized T84 colonic epithelial cells infected with EPEC and the indicated EspF mutants. The average change in TER in three independent experiments is shown. (B and C) Fluorescence microscopy of MDCK cells uninfected (B) or infected with EPEC for 4 h (C). Tight junction morphology was detected by anti-occludin immunocytochemistry. (D) Schematic of TAP tagged EspF is shown. Western blot of cellular lysates collected from stable MDCK cells expressing TAP-flag-EspF or mutant TAP-flag-EspF-D3. Anti-flag was used to probe EspF expression (top blot) and actin was used as a protein loading control (bottom blot). (E and F) Fluorescence microscopy of MDCK cells expressing TAP-EspF and TAP-EspF-D3. Tight junction morphology was detected by anti-occludin immunocytochemistry. (G) MDCK parental or Tap-EspF cellular lysates were incubated with anti-flag agarose and the resulting immuno-complexes were subjected to SDS-PAGE and stained with Coomassie. Proteins identified by mass spectrometry are indicated. "NS" designates nonspecific interacting proteins and "IgG LC" is the immunoglobulin light chain. (H) Anti-SNX9 immunofluorescence microscopy of $CaCo_2$ cells infected with the indicated EPEC strains for 3 h. Boxed area is a 4× magnification of the area indicated. Cellular borders are outlined. Bar = 15 μm. (I) Immunoblot of EspF from wild-type EPEC (Wt) or EPEC *espF*$^-$ strains carrying plasmids encoding wild-type EspF (*pespf*) or mutant EspF-D3 (*pespf-D3*) tagged with the myc epitope. Type III secreted EspF harvested from media supernatants (top) and from whole bacterial lysates (bottom) are shown. Concentrations of IPTG are indicated below.

Activation of SNX9 and N-WASP by EspF: a potential mechanism for signal amplification and specificity in eukaryotic cells

The major functional unit of EspF is composed of 3–5 highly conserved proline-rich repeat (PRR) domains of ∼47 amino acids. The purpose of the repeat sequences and how they confer a eukaryotic signaling response is largely unknown. Recently, EspF was shown to bind SNX9 through an SH3 domain interaction; however, the molecular details and the significance of this finding were left unexplored (Marches et al., 2006). We have expanded these initial observations by considering both the biochemical specificity of this protein–protein interaction and applying this knowledge to cellular models of EspF function. EspF possesses a single RxAPxxP motif at the N-terminal portion of each PRR domain that confers binding selectivity to the SH3 domain of SNX9. This configuration allows between three and five high affinity SNX9 bindings sites per EspF molecule.

Thus, the PRR domains may provide the bacterial effector a mechanism to increase protein avidity, or more interestingly, a means to amplify the SNX9 signal through oligomerization (Yarar et al., 2007). Consistent with these biochemical findings, engagement of the SNX9 SH3 domain by EspF induced robust membrane tubulation in cells. We now propose a concerted model for EspF function; direct binding to the SH3 domain of SNX9 transmits a membrane-remodeling signal to the C-terminal BAR domain. Importantly, similar membrane tubules have been observed upon expression of other BAR domain proteins (Peter et al., 2004), and we found that EspF-induced membrane tubulation did not occur with a BAR domain deletion mutant of SNX9. The potential importance and mechanism of these intramolecular interactions will be clarified as the EspF/SNX9 effector system is analyzed in biophysical detail.

Although we have focused primarily on the mechanisms of SNX9 activation by EspF, we have also discovered that EspF regulates actin cytoskeletal dynamics. In the context of the pyrene-actin assembly assay, the PRR domains in EspF are sufficient to induce N-WASP/Arp2/3 actin nucleation. EspF binds directly to the CRIB regulatory domain in N-WASP, a phenomenon similar to the reported mechanism of the Rho GTPase Cdc42. Similar findings have been previously reported for the functionally distinct PRR protein EspFu/TccP (Garmendia et al., 2006), indicating that both EspF and EspFu/TccP may use similar residues to independently activate N-WASP (Fig. 1). In addition, we have extended these findings by demonstrating that EspF nucleates a trimeric complex composed of SNX9 and N-WASP. This complex may provide EHEC 0157:H7 a potent mechanism for eukaryotic signal amplification and downstream signaling specificity during bacterial pathogenesis. For example, bacterial pedestals could be modified by EspFu/TccP activation of N-WASP (Campellone et al., 2004) while membrane trafficking would be regulated by EspF and the SNX9/N-WASP complex. This idea is particularly intriguing in light of studies by Yarar et al. (2007) that demonstrate the importance of SNX9 oligomerization to activate N-WASP during multiple modes of eukaryotic endocytosis.

EspF mimics an endogenous actin/membrane-signaling module to regulate membrane trafficking events

Genetic studies have linked EspF activity to a wide range of biological activities, including mitochondrial apoptosis (Crane et al., 2001; Nougayrede and Donnenberg, 2004), epithelial barrier disruption (McNamara et al., 2001), apical microvilli effacement (Dean et al., 2006), and inhibition of macrophage phagocytosis (Quitard et al., 2006). We found EspF to be necessary but not sufficient to regulate epithelial tight junction architecture during bacterial pathogenesis (see Fig. 7), suggesting that the EspF phenotypes observed in bacterial genetic studies may result from the concerted actions of several type III effector proteins or additional bacterial signaling mechanisms (Dean et al., 2006). Taking an alternative approach to bacterial genetics, we found that purified EspF binds directly to SNX9 in vitro and activates N-WASP in reconstitution assays. These activities could have direct and profound effects on membrane trafficking and the overall homeostasis of infected intestinal epithelial cells. For example, a recent report suggests that the Aquaporin (AQP) water channels are mislocalized during A/E pathogen infection, and this phenotype requires EspF expression (Guttman et al., 2007). In addition, EspF promotes the internalization of tight junction proteins in vivo (Guttman et al., 2006), potentially through a membrane-trafficking phenotype. These possibilities are consistent with our observed localization of EspF at clathrin structures, as membrane trafficking is required for epithelial tight junction maintenance and the formation of the apical/basolateral poles (Wells et al., 2006).

It is intriguing to note that the coordinated activation of SNX9 and N-WASP by EspF may actually represent a pathogenic strategy to mimic a natural host SNX9/N-WASP signaling complex. In earlier studies, our lab found that the *Drosophila* SNX9 (DSH3PX1) links axonal guidance receptors directly to N-WASP and the actin cytoskeleton (Worby et al., 2001). In addition, more recent studies suggest that engagement of the T cell antigen receptor (TCR) combined with costimulation of CD28 evoked the formation of a SNX9/WASP complex at endocytic sites of T cells (Badour et al., 2007). Together, these data establish the importance of an endogenous SNX9 and N-WASP signaling complex to regulate diverse eukaryotic trafficking events. Importantly, the functional link between these proteins may extend beyond clathrin-mediated endocytosis. Yarar et al. (2007) have described a mechanism in which SNX9 directly activates N-WASP for the purpose of regulating dorsal membrane ruffles, clathrin-independent fluid-phase endocytosis, and uptake of GPI-anchored proteins. Thus, our data suggest for the first time that EspF hijacks an endogenous SNX9/N-WASP signaling complex involved in multiple host cellular regulatory pathways.

Materials and methods

Plasmids

The *espf* gene from EHEC O157:H7 (GenBank accession no.#AP002566) and the EPEC E2348/69 *espf* were PCR cloned in-frame into pEGFP-C2 (CLONTECH Laboratories, Inc.). The *espfu/tccp* gene was cloned from a clinical isolate of EHEC 0157:H7 and has the sequence identical to GI: 15831969. The yeast two-hybrid clone of mouse SNX9 (NM_025664) residues 1–111, as well as full-length human SNX9, N-WASP, Grb2, NckI, and Nck2 were Topo cloned into pcDNA3.1-V5-His (Invitrogen). To produce mCherry-SNX9, the EGFP from pEGFP-C1 was replaced with mCherry by PCR subcloning. For bacterial expression, 47 amino acid N-terminal deletions (ΔN47) of EspF were PCR subcloned into pGEX-4T1 (GST-tag) (GE Healthcare) or pet30A (6xHis tag) (Novagen). EspF-D3 was generated with Multi-site QuikChange Site-Directed Mutagenesis (Stratagene) following the manufacturer's instructions. For bacterial complementation, the EPEC *espf* or mutant *espf-D3* was Topo cloned into pTrcHis2 with a *c-myc* epitope tag (Invitrogen). GST and His-tagged mini-N-WASP were obtained from Wendall Lim (University of California, San Francisco, San Francisco, CA; Prehoda et al., 2000). All constructs were verified by DNA sequencing.

Yeast two-hybrid

The yeast expression vector pLexA encoded a gene with N-terminal LexA binding domain and residues 1–248 of EHEC EspF. 250 μg of a d 9.5 and 10.5 mouse embryo library in VP16 were screened using the yeast two-hybrid system as previously described (Alto et al., 2006).

Cell culture, transfection, and wide-field fluorescence microscopy

Cell culture, transfections, and wide-field fluorescence microscopy was performed as previously described (Alto et al., 2006). Images were acquired on a microscope (Axiovert; Carl Zeiss Microimaging, Inc.) using a digital camera (MicroMax; Roper-Princeton Instruments) controlled by MetaFluor software

(Universal Imaging, Corp.). Optical filters were obtained from Chroma Technologies and 40 or 63× objectives were used for image acquisition.

Antibodies

Concentrations of anti-GFP polyclonal and monoclonal (CLONTECH Laboratories, Inc.), anti-His (QIAGEN), anti-GST, anti-flag M2, anti-flag polyclonal (Sigma-Aldrich), anti-HA (Covance), and anti-occludin (Zymed Laboratories) were used for immunoprecipitation, immunocytochemistry, and immunoblotting as recommended by the manufacturer. Rabbit polyclonal SNX9 antibody was used at 1:200 (Soulet et al., 2005). Rabbit polyclonal EspF was used at 1:10,000 (McNamara et al., 2001). Anti-tubulin antibody was used at 1:200 (Sigma-Aldrich), and Latrunculin-A at 1 μM (Calbiochem).

Recombinant protein production and GST pull-down assays

Recombinant 6×His EspFΔ47, mini-N-WASP (from Wendall Lim), N-WASP ΔEVH1 (from Jack Taunton; University of California, San Francisco, San Francisco, CA) and SNX9 were produced in BL-21/DE3 *E. coli* strain following standard methods. Cells were lysed in either His buffer (50 mM Tris, pH 7.4, 300 mM NaCl, 10 mM imidazole, and 0.5% Triton-X 100) or GST buffer (phosphate-buffered saline) supplemented with protease cocktail (Roche). Proteins were purified with Nickel agarose (QIAGEN) or glutathione-Sepharose (GE Healthcare) following the manufacturer's instructions. Proteins were dialyzed overnight in 2 l of lysis buffer at 4°C. Glycerol was added to 30% and aliquots were stored at −80°C. For GST pull-down assays, 10 μg of recombinant GST proteins immobilized to glutathione-Sepharose was incubated with 50 μl of [^{35}S]-methionine (GE Healthcare) produced with TNT reaction (Promega) for 4 h at 4°C. Proteins were separated by SDS-PAGE, dried, and exposed by autoradiography.

Peptide array and SNX9 overlay

Immobilized peptides were synthesized on cellulose paper using a Multipep Autospot synthesis robot following the manufacturer's directions (Intavis AG). Membranes were blocked in 5% milk in TBS-Tween. 50 μl of [^{35}S]-methionine SNX9 produced by TNT (Promega) was added to 5 ml of block solution and overlayed onto peptide membranes for 4 h at room temperature. Membranes were washed 3× 10 min in TBS-T and exposed by autoradiography.

Fluorescence polarization

FITC-labeled peptides (Cell Essentials) used for fluorescence polarization include EspF residues 69–86 (FITC-ATSFTPSRPAPPPTSGQA) or control peptide (FITC-QIAKRRRLSSLRA). Peptides (5 nM) were suspended to working dilutions in PBS with 5 mg/ml BSA. Increasing concentrations of purified GST-SNX9-SH3 or control GST proteins were mixed with peptides in 100 μl and incubated at room temperature for 10 min. Fluorescence polarization (FP) was measured on a GENios Pro (TECAN) fitted with FP excitation and emission filters, 485/535 nm. Polarization values (mP) were determined at equilibrium and normalized to the highest value of saturation. Saturation binding curve was generated with PRISM software (Graph Pad) and dissociation constants (K_D) were calculated from the nonlinear regression curve from averages of three independent experiments.

Phage display

A library of random dodecapeptides fused to the N terminus of the M13 gene-8 major coat protein was constructed and cycled through rounds of binding selections with the bacterially expressed SH3 domain immobilized on 96-well Maxisorp immunoplates (NUNC), as described previously (Sidhu et al., 2000; Laura et al., 2002). After four rounds of selection, individual phage were isolated and analyzed in a phage ELISA. Phage that bound to the SH3 domain was subjected to DNA sequence analysis.

Actin polymerization assays

1:1 mix of pyrene actin (~40% labeled, final is ~20% labeled) to cold G-actin (Cytoskeleton, Inc.) were mixed in G-buffer (5 mM Tris, pH 8.0, 0.2 mM $CaCl_2$, 0.2 mM ATP, and 1 mM DTT) and centrifuged at 100,000 *g* for 2 h. A final of 2.5 μM pyrene actin mix was added to 270 μl of Arp2/3 buffer (20 mM Tris, pH 7.5, 25 mM KCl, 1 mM $MgCl_2$, 0.1 mM ATP, and 1 mM ATP). 40 nm bovine Arp2/3 (a gift from Tom Pollard; Yale University, New Haven, CT) and 100 nM mini-N-WASP or N-WASP ΔEVH1 was mixed with various concentrations of GST, GST-EspF, or SNX9 constructs in 30 μl of 10× actin polymerization buffer (100 mM Tris, pH 7.5, 500 mM KCl, 20 mM $MgCl_2$, and 10 mM ATP). 270 μl pyrene actin (2.5 μM) was mixed with 30 μl mini-N-WASP-Arp2/3 and actin-assembly kinetics was monitored by pyrene fluorescence over a 10–20-min time interval. Peak fluorescence values were normalized to 2.4 μM actin consumption and graphed with PRISM Software.

Total internal reflection fluorescence microscopy (TIR-FM)

TIR-FM imaging procedures and microscopic manipulations were conducted as previously reported (Yarar et al., 2005). Swiss 3T3 cells stably expressing clathrin-light chain DsRed (Merrifield et al., 2002) were grown to 70% confluency in a 100-mm tissue culture dish in DME + 10% fetal calf serum and transfected with 20 μg EGFP-EspF or EGFP-EspF-D3 DNA using Lipofectamine 2000 (Invitrogen) according to the manufacturer's instructions. Cells were allowed to recover in fresh medium for 2 h, replated onto 22 × 22-mm, no. 1.5 glass coverslips (Corning; $n = 1.523$), and filmed the following morning.

Total internal reflection fluorescence (TIRF) microscopy was performed using an inverted microscope (TE2000U; Nikon) custom-modified to allow for through-the-objective multispectral total-internal reflection fluorescence microscopy using a 100×, 1.45 NA objective (Nikon), as previously described (Yarar et al., 2005). TIRF images were taken for 10 min at 2–3-s intervals, with a 100–300-ms exposure time, depending on the intensity of the signal.

Image analysis

Low expressing EGFP-EspF or EGFP-EspF-D3 cells stably expressing Clc-DsRed were chosen for ~8–12 min time-lapse movies. Stacks of red (Clc-DsRed) and green (GFP-EspF) images were de-interleaved into separate stacks. Clc-DsRed stacks were analyzed for candidate clathrin structures that were stable for 30 s before disappearance and seemed likely to represent single CCPs. Clathrin structures were excluded similar to the criteria described previously (Merrifield et al., 2002). We marked the position of each Clc-DsRed candidate with a ~1–2-μm diameter circle and observed GFP-EspF dynamics at these sites. This procedure yielded the coordinates of the CCS in both the red and green channels so that red and green regions precisely centered on the CCS could be excised and stored as mini-stacks for analysis. All time and fluorescence intensity measurements were based on these criteria. Image analysis was done with Metamorph (Universal Imaging Corp), Excel, and graphed using PRISM (Graph Pad).

To measure 25 CCPs, we first chose 25 candidate CCPs from 8 different cells. Each CCP appeared during the 10-min video series was stable for at least 30 s, disappeared from the evanescent field, and did not reappear for the remainder of the video series. The peak fluorescence intensity measurements were collected for each individual EspF and clathrin image and averaged background values were subtracted. Clathrin results were normalized to the mean fluorescence during the 21 s (7 frames) before the peak clathrin fluorescence (Merrifield et al., 2002). The time of clathrin departure (time 0) was defined as the last frame in which the normalized fluorescence value was within 90% of peak fluorescence and the signal reached <5% over the following 45 s of imaging. Each clathrin event ($n = 25$) was aligned to the time of departure and averaged. For EspF, the results of each event were normalized to the mean of three contiguous intensity values, including the peak value, then aligned to the time of clathrin departure and finally averaged (Merrifield et al., 2002). Kymograph analysis was performed using MetaMorph software.

EPEC infection experiments

T84 colonic epithelial cells were cultured and TER experiments were performed as described previously (McNamara et al., 2001). EPEC and *espF*$^-$ mutant strains (McNamara and Donnenberg, 1998) were complemented with plasmid EspF subcloned into pTrcHis2 (Invitrogen). Plasmid EspF was expressed in EPEC by incubation with 100 μM IPTG for 3 h before EPEC infections. T84 cells were infected with an MOI of 100 for the indicated time points. $CaCo_2$ experiments were performed by infecting cells with EPEC or the indicated mutants for 4 h before fixation and immunofluorescence processing.

MDCK stable cell lines and mass spectrometry

TAP-tagged EspF or mutant EspF-D3 were subcloned into pCDNA4T/O and MDCK stable cell lines were generated following the manufacturer's instructions (Invitrogen). Clonal lines expressing TAP-EspF or TAP-EspF-D3 were selected with 500 μg/ml zeocin and confirmed by Western blot and immunofluorescence microscopy. Purification of TAP-EspF was performed as follows: MDCK cells were lysed in 50 mM Hepes, pH 7.5, 150 mM NaCl, 5% glycerol, 0.5% TX-100, 1.5 mM $MgCl_2$, and 1 mM EGTA and incubated with anti-flag M2 beads for 2 h. The beads were washed 3× 10 min with lysis buffer and eluted with LDS-PAGE buffer (Invitrogen). Immunocomplexes were run down SDS-PAGE and gels were stained with Coomassie. Proteins were in-gel digested and analyzed with nano liquid chromatography tandem mass spectrometry. Acquired data was searched

with Inspect against a dog database (National Center for Biotechnology Information, Canis familiaris fasta protein database). Identified peptides were manually verified to be canine SNX9: aa 218–237, SAAPYFKDSESAEAGGAQR; aa 313–327, SYIEYQLTPTNTNR; aa 346–359, FGSAIPIPSLPDK; aa 515–529, TYEEIAGLVAEQPK; aa 543–557, K.GFLGCFPDIIGAHK.G; and aa 605–613, IYDYNSVIR.

Online supplemental material

Fig. S1 shows membrane tubule formation induced by EspF, and colocalization of endogenous SNX9 at these sites (Fig. S1, A and B). Fig. S2 demonstrates that actin is polymerized de novo at sites of EspF/SNX9 membrane tubules. Video 1 shows dynamics of EGFP-EspF and Clc-DsRed in living Swiss 3T3 cells captured by TIR-FM. Video 2 shows EspF and clathrin dynamics at a single CCP. Video 3 shows a dynamic membrane tubule induced by EspF expressing at the cell surface. Video 4 demonstrates a "rocketing" clathrin structures seemingly being propelled by EspF. Video 5 demonstrates a splitting clathrin structures with EspF localizing to the center of this event.

We would like to thank C.J. Allison, Timo Meerloo, and Ingrid Niesman for expert technical assistance. Critical reagents were provided by Wendall Lim and Tom Pollard, for which we are grateful. We would like to thank members of the Dixon lab for critical reading of this manuscript and for helpful scientific discussions.

This research was supported by Grants from the National Institutes of Health, the Walther Cancer Institute, the Ellison Foundation, and the Howard Hughes Medical Institute (to J.E. Dixon). N.M. Alto was supported by Hematology and Diabetes National Institutes of Health training grants. Grants from NCIC support C. Boone and R. Tonikian.

Submitted: 4 May 2007
Accepted: 27 August 2007

References

Alto, N.M., F. Shao, C.S. Lazar, R.L. Brost, G. Chua, S. Mattoo, S.A. McMahon, P. Ghosh, T.R. Hughes, C. Boone, and J.E. Dixon. 2006. Identification of a bacterial type III effector family with G protein mimicry functions. *Cell.* 124:133–145.

Badour, K., M.K. McGavin, J. Zhang, S. Freeman, C. Vieira, D. Filipp, M. Julius, G.B. Mills, and K.A. Siminovitch. 2007. Interaction of the Wiskott-Aldrich syndrome protein with sorting nexin 9 is required for CD28 endocytosis and cosignaling in T cells. *Proc. Natl. Acad. Sci. USA.* 104:1593–1598.

Benesch, S., S. Polo, F.P. Lai, K.I. Anderson, T.E. Stradal, J. Wehland, and K. Rottner. 2005. N-WASP deficiency impairs EGF internalization and actin assembly at clathrin-coated pits. *J. Cell Sci.* 118:3103–3115.

Campellone, K.G., D. Robbins, and J.M. Leong. 2004. EspFU is a translocated EHEC effector that interacts with Tir and N-WASP and promotes Nck-independent actin assembly. *Dev. Cell.* 7:217–228.

Co, C., D.T. Wong, S. Gierke, V. Chang, and J. Taunton. 2007. Mechanism of actin network attachment to moving membranes: barbed end capture by N-WASP WH2 domains. *Cell.* 128:901–913.

Cornelis, G.R., and F. Van Gijsegem. 2000. Assembly and function of type III secretory systems. *Annu. Rev. Microbiol.* 54:735–774.

Crane, J.K., B.P. McNamara, and M.S. Donnenberg. 2001. Role of EspF in host cell death induced by enteropathogenic Escherichia coli. *Cell. Microbiol.* 3:197–211.

Dean, P., and B. Kenny. 2004. Intestinal barrier dysfunction by enteropathogenic Escherichia coli is mediated by two effector molecules and a bacterial surface protein. *Mol. Microbiol.* 54:665–675.

Dean, P., M. Maresca, S. Schuller, A.D. Phillips, and B. Kenny. 2006. Potent diarrheagenic mechanism mediated by the cooperative action of three enteropathogenic Escherichia coli-injected effector proteins. *Proc. Natl. Acad. Sci. USA.* 103:1876–1881.

Galan, J.E., and A. Collmer. 1999. Type III secretion machines: bacterial devices for protein delivery into host cells. *Science.* 284:1322–1328.

Garmendia, J., A.D. Phillips, M.F. Carlier, Y. Chong, S. Schuller, O. Marches, S. Dahan, E. Oswald, R.K. Shaw, S. Knutton, and G. Frankel. 2004. TccP is an enterohaemorrhagic Escherichia coli O157:H7 type III effector protein that couples Tir to the actin-cytoskeleton. *Cell. Microbiol.* 6:1167–1183.

Garmendia, J., M.F. Carlier, C. Egile, D. Didry, and G. Frankel. 2006. Characterization of TccP-mediated N-WASP activation during enterohaemorrhagic Escherichia coli infection. *Cell. Microbiol.* 8:1444–1455.

Gruenheid, S., and B.B. Finlay. 2003. Microbial pathogenesis and cytoskeletal function. *Nature.* 422:775–781.

Guttman, J.A., F.N. Samji, Y. Li, A.W. Vogl, and B.B. Finlay. 2006. Evidence that tight junctions are disrupted due to intimate bacterial contact and not inflammation during attaching and effacing pathogen infection in vivo. *Infect. Immun.* 74:6075–6084.

Guttman, J.A., F.N. Samji, Y. Li, W. Deng, A. Lin, and B.B. Finlay. 2007. Aquaporins contribute to diarrhoea caused by attaching and effacing bacterial pathogens. *Cell. Microbiol.* 9:131–141.

Higgs, H.N., and T.D. Pollard. 2001. Regulation of actin filament network formation through ARP2/3 complex: activation by a diverse array of proteins. *Annu. Rev. Biochem.* 70:649–676.

Innocenti, M., S. Gerboth, K. Rottner, F.P. Lai, M. Hertzog, T.E. Stradal, E. Frittoli, D. Didry, S. Polo, A. Disanza, et al. 2005. Abi1 regulates the activity of N-WASP and WAVE in distinct actin-based processes. *Nat. Cell Biol.* 7:969–976.

Kaksonen, M., C.P. Toret, and D.G. Drubin. 2005. A modular design for the clathrin- and actin-mediated endocytosis machinery. *Cell.* 123:305–320.

Kaksonen, M., C.P. Toret, and D.G. Drubin. 2006. Harnessing actin dynamics for clathrin-mediated endocytosis. *Nat. Rev. Mol. Cell Biol.* 7:404–414.

Laura, R.P., A.S. Witt, H.A. Held, R. Gerstner, K. Deshayes, M.F. Koehler, K.S. Kosik, S.S. Sidhu, and L.A. Lasky. 2002. The Erbin PDZ domain binds with high affinity and specificity to the carboxyl termini of delta-catenin and ARVCF. *J. Biol. Chem.* 277:12906–12914.

Lundmark, R., and S.R. Carlsson. 2003. Sorting nexin 9 participates in clathrin-mediated endocytosis through interactions with the core components. *J. Biol. Chem.* 278:46772–46781.

Marches, O., M. Batchelor, R.K. Shaw, A. Patel, N. Cummings, T. Nagai, C. Sasakawa, S.R. Carlsson, R. Lundmark, C. Cougoule, et al. 2006. EspF of enteropathogenic Escherichia coli binds sorting nexin 9. *J. Bacteriol.* 188:3110–3115.

McNamara, B.P., and M.S. Donnenberg. 1998. A novel proline-rich protein, EspF, is secreted from enteropathogenic Escherichia coli via the type III export pathway. *FEMS Microbiol. Lett.* 166:71–78.

McNamara, B.P., A. Koutsouris, C.B. O'Connell, J.P. Nougayrede, M.S. Donnenberg, and G. Hecht. 2001. Translocated EspF protein from enteropathogenic Escherichia coli disrupts host intestinal barrier function. *J. Clin. Invest.* 107:621–629.

Merrifield, C.J., S.E. Moss, C. Ballestrem, B.A. Imhof, G. Giese, I. Wunderlich, and W. Almers. 1999. Endocytic vesicles move at the tips of actin tails in cultured mast cells. *Nat. Cell Biol.* 1:72–74.

Merrifield, C.J., M.E. Feldman, L. Wan, and W. Almers. 2002. Imaging actin and dynamin recruitment during invagination of single clathrin-coated pits. *Nat. Cell Biol.* 4:691–698.

Merrifield, C.J., B. Qualmann, M.M. Kessels, and W. Almers. 2004. Neural Wiskott Aldrich Syndrome Protein (N-WASP) and the Arp2/3 complex are recruited to sites of clathrin-mediated endocytosis in cultured fibroblasts. *Eur. J. Cell Biol.* 83:13–18.

Merrifield, C.J., D. Perrais, and D. Zenisek. 2005. Coupling between clathrin-coated-pit invagination, cortactin recruitment, and membrane scission observed in live cells. *Cell.* 121:593–606.

Miki, H., T. Sasaki, Y. Takai, and T. Takenawa. 1998. Induction of filopodium formation by a WASP-related actin-depolymerizing protein N-WASP. *Nature.* 391:93–96.

Nougayrede, J.P., and M.S. Donnenberg. 2004. Enteropathogenic Escherichia coli EspF is targeted to mitochondria and is required to initiate the mitochondrial death pathway. *Cell. Microbiol.* 6:1097–1111.

Peter, B.J., H.M. Kent, I.G. Mills, Y. Vallis, P.J. Butler, P.R. Evans, and H.T. McMahon. 2004. BAR domains as sensors of membrane curvature: the amphiphysin BAR structure. *Science.* 303:495–499.

Prehoda, K.E., J.A. Scott, R.D. Mullins, and W.A. Lim. 2000. Integration of multiple signals through cooperative regulation of the N-WASP-Arp2/3 complex. *Science.* 290:801–806.

Quitard, S., P. Dean, M. Maresca, and B. Kenny. 2006. The enteropathogenic Escherichia coli EspF effector molecule inhibits PI-3 kinase-mediated uptake independently of mitochondrial targeting. *Cell. Microbiol.* 8:972–981.

Shifflett, D.E., D.R. Clayburgh, A. Koutsouris, J.R. Turner, and G.A. Hecht. 2005. Enteropathogenic E. coli disrupts tight junction barrier function and structure in vivo. *Lab. Invest.* 85:1308–1324.

Sidhu, S.S., H.B. Lowman, B.C. Cunningham, and J.A. Wells. 2000. Phage display for selection of novel binding peptides. *Methods Enzymol.* 328:333–363.

Soulet, F., D. Yarar, M. Leonard, and S.L. Schmid. 2005. SNX9 regulates dynamin assembly and is required for efficient clathrin-mediated endocytosis. *Mol. Biol. Cell.* 16:2058–2067.

Steyer, J.A., and W. Almers. 2001. A real-time view of life within 100 nm of the plasma membrane. *Nat. Rev. Mol. Cell Biol.* 2:268–275.

Theriot, J.A., T.J. Mitchison, L.G. Tilney, and D.A. Portnoy. 1992. The rate of actin-based motility of intracellular Listeria monocytogenes equals the rate of actin polymerization. *Nature.* 357:257–260.

Veiga, E., and P. Cossart. 2006. The role of clathrin-dependent endocytosis in bacterial internalization. *Trends Cell Biol.* 16:499–504.

Viswanathan, V.K., A. Koutsouris, S. Lukic, M. Pilkinton, I. Simonovic, M. Simonovic, and G. Hecht. 2004. Comparative analysis of EspF from enteropathogenic and enterohemorrhagic Escherichia coli in alteration of epithelial barrier function. *Infect. Immun.* 72:3218–3227.

Wells, C.D., J.P. Fawcett, A. Traweger, Y. Yamanaka, M. Goudreault, K. Elder, S. Kulkarni, G. Gish, C. Virag, C. Lim, et al. 2006. A Rich1/Amot complex regulates the Cdc42 GTPase and apical-polarity proteins in epithelial cells. *Cell.* 125:535–548.

Worby, C.A., N. Simonson-Leff, J.C. Clemens, R.P. Kruger, M. Muda, and J.E. Dixon. 2001. The sorting nexin, DSH3PX1, connects the axonal guidance receptor, Dscam, to the actin cytoskeleton. *J. Biol. Chem.* 276:41782–41789.

Yarar, D., C.M. Waterman-Storer, and S.L. Schmid. 2005. A dynamic actin cytoskeleton functions at multiple stages of clathrin-mediated endocytosis. *Mol. Biol. Cell.* 16:964–975.

Yarar, D., C.M. Waterman-Storer, and S.L. Schmid. 2007. SNX9 couples actin assembly to phosphoinositide signals and is required for membrane remodeling during endocytosis. *Dev. Cell.* 13:43–56.